2012

Prediction of Droplet Dynamics on an Incline

S. R. Annapragada
Purdue University

J. Y. Murthy
Purdue University

S V. Garimella
Purdue University, sureshg@purdue.edu

Annapragada, S. R.; Murthy, J. Y.; and Garimella, S V., "Prediction of Droplet Dynamics on an Incline" (2012). *CTRC Research Publications.* Paper 161.
http://dx.doi.org/doi:10.1016/j.ijheatmasstransfer.2011.10.028

Prediction of Droplet Dynamics on an Incline

S. Ravi Annapragada, Jayathi Y. Murthy and Suresh V. Garimella
Cooling Technologies Research Center, an NSF IUCRC
School of Mechanical Engineering and Birck Nanotechnology Center
Purdue University
West Lafayette, Indiana 47907-2088 USA
{asravi, jmurthy, sureshg}@purdue.edu

Corresponding Author: Suresh V. Garimella, Tel: +1 765 494 5621

1. INTRODUCTION

Droplet transport is critical in self-cleaning applications [1], microassays [2] and microfluidic devices [3]. The main advantage of miniaturizing assays and bioanalytical tools include improved performance, speed and reduced costs, as well as the ability to perform parallel and integrated analysis [4-6]. Hydrophobic coatings aid in the reduction of retarding forces (surface tension and viscous forces) on the droplet [7]. A careful study of the droplet motion on hydrophobic surfaces is essential to understanding and improving performance in these applications.

There has been a long-standing debate on whether a droplet rolls or slides down an inclined surface. Yarnold [8] was the first to visualize the fluid flow on the surface of a mercury droplet by observing the dust particles on the droplet as it slid down an incline. Based on these observations, Yarnold proposed that the velocity of the top surface was greater than the net droplet motion, and hence the droplet appeared to roll. Allen and Benson [9] later injected a dye into mercury to visualize the droplet motion down an incline and found similar results.

More recently, the motion of water droplets on hydrophobic surfaces has been investigated [9-14]. The droplet motion was captured using high-speed visualization coupled with image analysis. Sakai *et al.* [10] studied the rolling/sliding behavior of water droplets on a variety of hydrophobic surfaces. They determined the rolling versus sliding behavior of water based on the motion of single indicator particles entrained in the droplets. A similar technique was used by Song [11] to study water droplet motion on superhydrophobic methyl-terminated organosilane-modified silicon wafer surfaces. The droplet size and surface hydrophobicity were found to determine the mode of droplet motion.

Sakai *et al.* [12] employed Particle Image Velocimetry (PIV) to visualize the internal fluidity of droplets sliding down hydrophobic surfaces. The PIV analysis was further used by Suzuki *et al.* [13] to understand the slipping and rolling components of the sliding velocity and acceleration of water droplets, based on the motion of the advancing edge and the PIV analysis, respectively. Sakai *et al.* [14] measured advancing and receding angles at two different flow rates using the so-called expansion and contraction method. The advancing angle was seen to decrease as the radius of the droplet increased. Although not noted in the paper, this is likely due to the decreased droplet velocity at larger radii for a given flow rate, which would reduce the contact angle. The velocity dependence of contact angle, which has been shown to be important in [15], was measured. All the measurements were made at the center plane of the droplet and hence the three-dimensional flow pattern could not be identified.

Various numerical methods are in use to study multiphase flows and the interfacial phenomena involved. These include Arbitrary Lagrangian Eulerian (ALE) techniques [16], the boundary integral method [17], adaptive grid methods [18], and fixed grid techniques such as the level set [19] and the volume of fluid (VOF) [20] methods. The VOF approach has been among the more popular tools for studying bubble and droplet dynamics [21].

Afkhami *et al.* [22] developed a height function-based VOF model and showed the use of VOF in predicting droplet shape during impact on a flat surface and droplet motion down an incline [23]. The effect of inclination angle on the shape of the droplet and the contact angle distribution along the contact line was determined. The implementation of a dynamic contact angle model was presented but no experimental comparisons were made. Further, the surface considered was not hydrophobic. To the authors' knowledge, experimentally validated simulations of droplets sliding on hydrophobic surfaces do not appear to be available in the literature. In related work by the authors, VOF simulations of sessile, static droplets on an incline were compared to experimental measurements [24]. Droplet shape and critical sliding angle were predicted for different sizes of water droplets resting on a smooth PTFE (polytetrafluoroethylene) surface. Predictions of the critical inclination angle for sliding were found to be within 1° of the experimental measurements. These studies indicate that the VOF technique can be a useful technique in understanding droplet dynamics.

In the present work, we consider the internal fluid motion in droplets moving at their terminal velocity on an inclined surface. Experimental observations of contact angles and terminal velocity of water droplets sliding on PTFE surfaces are first reported. A new approach to computing the terminal velocity condition using the VOF-CSF method is described. The numerical methodology is first verified against a two-dimensional stationary reference frame solution and then used to simulate water droplets sliding down a PTFE surface at terminal velocity; the resulting internal flow patterns are discussed.

2. MATERIALS AND METHODS

Experimental measurements of the droplet profile and the advancing and receding contact angles are obtained at different droplet sizes and surface inclinations. The test surfaces used in the experiments are identical to those described in Annapragada *et al.* [24]. The experimental setup consists of a movable tilt stage for mounting the test surfaces, along with a high-speed camera for imaging from the side. The working fluid is de-ionized water. The surface is tilted to the desired angle of inclination and the experiment is initiated by dispensing a known volume of liquid gently on the PTFE-coated glass slide

upstream of the field of view of the camera. The droplet attains terminal velocity before it passes through the field of view of the camera. This is verified by ensuring that the velocity remains constant as the droplet passes through the field of view of the camera. Images are captured at 1000 fps using a high-speed camera (Photron Fastcam Ultima APX). The experimental setup is shown in Figure 1. The images are post-processed using MATLAB [25] to obtain the droplet profile and advancing and receding contact angles. The uncertainty in volume measurement of a 10 µl droplet is 24 μm^3 (24 x 10^{-6} µl). The velocities are obtained by tracking the leading and trailing edge of the droplet.

3. NUMERICAL SIMULATION

In the current work the VOF-CSF framework in FLUENT [26] is used. A custom contact-angle model is implemented by means of user-defined functions to capture the contact angle variation as a function of velocity. A pseudo-Lagrangian methodology, described below, is developed to reduce the domain size and hence the computational time. The VOF-CSF method itself is described in detail in Annapragada *et al.* [24]. In the current model, volume fraction smoothing is used to reduce the spurious velocities at the interface associated with the VOF method [27,28]. Smoothing is performed by averaging the volume fraction based on the neighboring cell volume fractions. However, over-smoothing could result in smearing of the interface to more than two cells. A smoothing relaxation value of 0.25 to prevent over-smoothing was found to be optimal.

3.1. Pseudo-Lagrangian Methodology

The VOF method belongs to the class of Eulerian methods which are characterized by a stationary mesh. The droplet motion simulations require a large computational domain spanning tens of droplet lengths to simulate a droplet starting from a stationary state and reaching terminal velocity. The droplet at any point of time occupies only a small part of this domain and the computations in the domain far from the droplet do not affect the droplet motion but add to computational time. This problem is avoided by shifting to a moving reference frame. The new methodology developed here computes the flow in a reference frame following the droplet. This allows a much smaller domain to be used and reduces the computational time per iteration. In this reference frame, the droplet would appear stationary and the surface below and the air around the droplet move in a direction opposite to that of the droplet motion. A no-slip boundary condition with a time-varying velocity profile is specified at the bottom wall. The velocity of this wall is updated at each time step to render the droplet stationary. Terminal velocity is considered to have been reached when no further updates of the wall velocity are necessary.

The flowchart for the methodology is shown in Figure 2. The leading and the trailing edges are tracked as a function of time. For the calculation of terminal velocity, the droplet location is approximated as the average of the leading and trailing edge locations. Since the spatial resolution is no better than one computational cell, the location of the leading or trailing edge is taken to be that of the cell center in which the leading or trailing edge is respectively present. Hence a droplet is said to move only when the edge of the droplet changes cell location. The velocity of the reference frame, *i.e.*, the surface and air velocity, are updated based on the change in droplet location given by:

$$V_T = V_{T0} + C_V . \left(\frac{l_{drop} - l_{drop0}}{\Delta t} \right) \tag{1}$$

where C_V is a constant, V_T is the current reference frame velocity and V_{T0} is the reference velocity at the previous time step. The velocities in the domain are shifted to the new reference frame as:

$$\vec{V}_{cell} = \vec{V}_{cell0} + (V_T - V_{T0})\hat{i} \tag{2}$$

Since the reference velocity of the domain changes over time, the current reference frame is treated as an accelerating reference frame. Hence a pseudo-force is included as a source term in the discrete *i* momentum equation, and is given by:

$$F_{cell} = \rho \forall \frac{(V_T - V_{T0})}{\Delta t} \tag{3}$$

In the current methodology the reference frame lags the droplet motion by one time step in updating the reference frame. When the droplet reaches terminal velocity, the droplet reference frame and the numerical reference frame are identical and hence the droplet is stationary in the numerical reference frame. This is considered the final steady state in the droplet frame of reference.

3.2. Geometric Model and Initial and Boundary Conditions

A hybrid grid is used for the droplet simulations with square orthogonal cells in the region of the droplet motion and an unstructured grid farther away. Figure 3 shows the initial shape of the droplet along with the surrounding mesh at the symmetry plane. A hemispherical cap of the required droplet size and material is initialized in the domain. The droplet/air interface in the figure is shown at $\alpha = 0.5$ where α is the VOF volume fraction. Acceleration due to gravity is applied throughout the domain and is based on the angle of inclination of the surface being simulated. Utilizing droplet symmetry about the x-y plane (z = 0 mm), only half of the domain is modeled and the results mirrored for presentation. The solid surface at the bottom (y = 0 mm) along with the right-side boundary ($x = x_{max}$) are given a velocity V_T in the x-

direction. On boundaries at which flow leaves the domain, the specified pressure is treated as the stagnation pressure; at outflow boundaries ($x = x_{min}$), the specified pressure is assumed to be the static pressure [26]. The top boundary ($y = y_{max}$) is specified as a wall with zero shear simulating a far-field boundary.

3.3. Contact Angle Model Boundary Condition

The VOF-CSF model requires contact angles to be specified as a boundary condition, and therefore an accurate specification of the dynamic contact angle (DCA) variation along the contact line is necessary. To demonstrate the importance of the dynamic contact angle model, three different contact angle models are assessed by comparison against experimental measurements of terminal velocity obtained with water droplets moving down a smooth, inclined Teflon surface. The models are plotted as a function of the local capillary number along the contact line (Figure 4). The description of the models is as follows:

1. The two step static contact angle (SCA) model:

   In the SCA model, a fixed advancing contact angle is applied to the leading part ($\vec{v}_{CL}.\hat{n} > 0$) and a fixed receding contact angle to the trailing part ($\vec{v}_{CL}.\hat{n} < 0$) of the contact line, where $\vec{v}_{CL}$ is the local contact line velocity and $\hat{n}$ is the normal to the contact line.

2. The dynamic contact angle (DCA) model:

   The DCA model is based on the experimental measurements made in this work. Rio *et al.* [29] showed that the DCA along the interface depends only on the capillary number based on the velocity normal to the contact line. Hence, the DCA models developed for advancing and receding contact angles can be utilized to define contact angles all along the interface. The contact angle is specified as a function of the capillary number defined by

$$Ca = \frac{\mu(\vec{v}_{CL}.\hat{n})}{\sigma} \tag{4}$$

   where μ is the viscosity of the fluid, $\vec{v}_{CL}.\hat{n}$ the velocity normal to the triple contact line and σ is the surface tension of the water/air interface. The experimentally measured advancing and receding contact angles from experiments are given respectively by:

$$\frac{\cos\theta_{0,adv} - \cos\theta_{adv,dyn}}{\cos\theta_{0,adv} + 1} = 2.24 Ca^{0.54} \tag{5}$$

$$\frac{\cos\theta_{0,rec} - \cos\theta_{rec,dyn}}{\cos\theta_{0,rec} + 1} = \tanh\left(9 Ca^{0.702}\right) \tag{6}$$

where $\theta_{0,adv}$ = 121°, $\theta_{0,rec}$ = 104.5°. The correlations employ the local capillary number based on the velocity $\vec{v}_{CL}.\hat{n}$. Details of the experimental measurements are given in Section 4.

3. The mesh-dependent contact angle (MDCA) model:
   Although a no-slip boundary condition is applied at the droplet-solid wall interface in the VOF simulations, slip is required at the contact line for the droplet interface to move. Recently, Afkhami *et al.* [30] showed evidence of the dependence of the contact line motion on the grid size at the interface and proposed a mesh-dependent contact angle (MDCA) model to solve this mesh-dependence problem. Their correction to the DCA model is given by:

$$\cos(\theta_{num}) = \cos(\theta_{app}) + 5.63\text{Ca}\ln(\text{K}/(\Delta/2)) \quad (7)$$

   where K is a constant (with a dimension of length) that depends on the slip model, Δ is the grid size, θ_{num} is the applied contact angle and θ_{app} is the DCA. This model is based on the three-region theory (molecular region or slip region, intermediate region and macroscopic region) at the contact line proposed by Cox [31]. Cox matched asymptotic solutions between adjoining regions to arrive at a constitutive relation between the contact angle in the molecular region (contact angle at the wall) and that in the macroscopic region (θ_{app}). This dependence of contact angle on slip length has been shown earlier by many researchers [37-38, 44]. The correlations of Cox-Voinov [32] and Sheng and Zhou [33] were based on Cox's method. A brief review of the Cox theory is given in Afkhami *et al.* [30].

4. RESULTS AND DISCUSSION

Experimental results for the velocity-dependence of the advancing and receding contact angles for water droplets moving on a PTFE surface are presented. The modeling technique described above is validated against 2D stationary reference frame simulations. The model is then used to predict the droplet motion at terminal velocity for water on PTFE. The predicted terminal velocity and the associated droplet shapes are validated against the experimental results. The internal fluidity of the droplets at terminal velocity is briefly examined.

4.1. Experimental Observations

Images of de-ionized water droplets of 5, 7.5 and 10 µl volume are captured as they slide down the surface held at inclinations of β = 30°, 45° and 60° (Figure 5). Experiments were performed for all combinations of inclination angles and droplet volumes. However, results are only presented for those angles of inclination and droplet volumes for which the droplet experiences motion. The omitted test cases fall below the critical angle of inclination for the droplets and hence there is no droplet motion. As

β increases, the velocity increases, as does the advancing contact angle, while the receding contact angle decreases. This effectively increases the contact angle hysteresis, *i.e.*, the difference between the advancing and receding contact angles. The average contact angle of the water droplets on a horizontal PTFE surface is observed to be 120°, which matches previously reported measurements. The uncertainties in the measurement of contact angle and droplet velocities are estimated to be 1° and 0.01 m/s, respectively.

The measured contact angles, $\theta_{adv,dyn}$ and $\theta_{rec,dyn}$, are plotted against the capillary number in Figure 6. A number of dynamic contact angle (DCA) models are available in the literature, mainly for the advancing contact angle. Some of the important DCA correlation models [34-36] are summarized in TABLE 1. Predictions from the empirical DCA models are compared with the experimental measurements in Figure 7. The Seebergh and Berg [36] predictions best describe the advancing DCA measurements from the present work. However, this model cannot be applied to receding DCA prediction as it cannot handle negative capillary numbers. A similar difficulty exists for the Bracke *et al.* [34] and Jiang *et al.* [35] models. Hence the Seebergh and Berg model was used for the advancing contact angle in the present simulations and is given by Eq.(5). As the Jiang *et al.* [35] can handle negative capillary number, a curve fit to the experimental measurements based on the Jiang *et al.* model was used for the receding contact angle, as shown in Figure 6 and given by Eq.(6).

4.2. Numerical Results and Validation

4.2.1. 2D Droplet – Comparison between Droplet Reference Frame and Stationary Reference Frame

The simulations using the new methodology are first compared with stationary droplet simulations of a 2D droplet sliding on a vertical surface. A two-dimensional droplet of radius 1 mm resting on a vertical surface with $\theta_{rec} = \theta_{adv} = 120°$ is considered. A vertical body force acts on the droplet with an equivalent acceleration due to gravity of $g_{static} = 1.0$ m/s^2. The droplet slides along the surface and reaches steady-state terminal velocity. The Bond number ($Bo = \frac{\rho g d^2}{\sigma}$) for the droplet is 10. The droplet motion is simulated in a stationary reference frame and in the droplet reference frame using the proposed numerical methodology. Identical mesh densities with grid size of 0.1 mm × 0.1 mm in the droplet region are used for both simulations. A sample mesh for the droplet reference frame simulation is shown in Figure 8 with a grid count of 2800. Table 2 summarizes the results from the two simulations. The terminal velocity,

the distance travelled by the droplet in each simulation, and the simulation time are compared in the table. The two droplet velocity predictions are identical. The droplet in the stationary reference frame simulation requires a computation domain with 20,000 cells to reach terminal velocity. The computational time using the current numerical methodology reduces the simulation time seven-fold (on a 2.33 GHz Intel E5410 processor). The instantaneous location of the leading and trailing edges and the reference frame velocity for the droplet reference frame simulation are plotted as function of time in Figure 9. The fluctuations in the convergence behavior occur because of the relatively large velocity increment (C_v) of 0.015 m/s. Using a lower velocity increment was found to reduce the fluctuations. The required accuracy of velocity predictions and a reduction of the fluctuations in the convergence behavior are the criteria used in choosing the value of C_v. The velocity profiles inside the droplet in the reference frame of the droplet from the two simulations are compared in Figure 10. The maximum deviation in the velocity predictions is 3%, verifying the proposed numerical methodology.

4.2.2. Motion of Deionized Water Droplets on a Smooth PTFE Surface

The numerical model is used to simulate the motion of water droplets down a smooth PTFE surface. The physical properties used in the simulations are viscosity (μ) = 0.05 Pa.s, density (ρ) = 998 kg/m^3 and surface tension coefficient (σ) = 0.0728 N/m. A structured grid with over 30 grid points spanning the droplet diameter and 18 spanning the height of the droplet is used to simulate the droplet. The total cell count in the domain is 316,386 cells. The contact angle boundary condition imposed in the model is based on the experimental DCA correlations given in Eqs. (5) and (6). The capillary number in the correlations is based on the local normal contact line velocity. The parameter C_V in Eq.(1) is again chosen to increment the velocity of the reference frame by 0.01 m/s. This value is 7% of V_T for a 7.5 µl droplet sliding down a 60° incline, and is the resolution with which the terminal velocity can be determined in the current simulations.

The terminal velocity is computed for three different droplet volumes (5 µl, 7.5 µl and 10 µl) at a 60° incline and is compared to experimental results in Table 3. For the sake of brevity, validation cases are shown for varying droplet volume at a fixed angle of inclination. The relative deviation of the prediction from the experiment is also listed in the table. The predictions for higher capillary numbers match well with experiments. The lowest capillary number predictions deviate from the experiment by 50% but still are within experimental and numerical uncertainties. This large deviation is due to the extrapolation of the contact angle model to lower capillary numbers than for which it was developed. The applied contact angle thus deviates from the actual value, causing the simulation results to differ from the experiments.

The droplet shape, footprint, height and contact length are extracted for a 10 µl droplet moving down a $\beta = 45°$ incline, and predictions compared to experiment in Figure 11 and Table 4. The uncertainties in length in the experiments and the numerical simulations stem from the pixel resolution and the grid resolution and are 88 µm and 30 µm, respectively. The predicted droplet shape, and its length and height match the experiments to within the experimental and numerical uncertainties.

The contact line of the droplet extracted from the simulation is shown in Figure 12. The contact line is colored with the local contact angle value imposed as a boundary condition. The contact line deviates from a circular shape as the droplet stretches along the direction of motion.

4.2.3. Sensitivity of Results to Contact Angle Boundary Condition

The sensitivity of the droplet motion to uncertainties in the imposed contact angle from the experiments is investigated by considering a 7.5 µl droplet moving down an incline ($\beta = 60°$). Reducing the advancing contact angle by the amount of the experimental uncertainty of 0.5°, and increasing the receding contact angle by this same amount causes the predicted terminal velocity to increase by 25% to $V_T = 1.2$ m/s. A simulation with the advancing angle increased by 0.5° and the receding angle reduced by the same amount resulted in a reduction in terminal velocity by a similar factor.

The large sensitivity to contact angle is explained by analyzing the corresponding change in surface tension force at the contact line of a 2D droplet. The surface tension force acting on the droplet (F_{ST}) is given by:

$$F_{ST} = \sigma(\cos\theta_{rec} - \cos\theta_{adv}) \tag{8}$$

which, upon simplification, becomes $F_{ST} = \sigma \sin(\theta_{rec} + \theta_{adv}) \sin(\Delta\theta_h)$, where $\Delta\theta_h$ is the contact angle hysteresis. The contact angle hysteresis for the 7.5 µl droplet moving on a 60° incline is 8°±1°; this uncertainty represents a change in the value of $\sin(\Delta\theta_h)$ of 12.4%. Thus, for the low contact angle hysteresis characteristic of hydrophobic surfaces, significant sensitivity to contact angle values is to be expected. Hydrophilic surfaces with typically larger contact angle hysteresis would not be prone to this sensitivity.

Given this sensitivity to contact angle, terminal velocity predictions from the different contact angle models described above are compared in Table 5 for a 7.5 µl droplet moving on a 60° incline. Two

different meshes, of sizes 88 μm and 44 μm, were considered for the DCA and MDCA models. The overall cell counts were 316,386 and 1,265,544, respectively. All models predict the same droplet shape. The DCA and MDCA models also predict the experimental terminal velocity (0.12 m/s) well, but the SCA model underpredicts the terminal velocity by 3.5 times. Thus, it is recommended that both the droplet shape and the terminal velocity predictions should be validated against measurements.

The mesh-dependent contact angle model proposed by Afkhami *et al.* [20] was applied with values of K = 0.002. For the mesh sizes used, the applied contact angle changes by 0.5° when the mesh-dependent model was applied. A grid refinement study was carried out in which the mesh dependent model was evaluated with two levels of successively refined meshes with uniform grid sizes of 88 μm and 44 μm in the vicinity of the interface. The terminal velocity results with these grids are shown after steady state is reached (Table 5). The velocity predictions for both meshes are within the experimental uncertainty. The results of the grid independence study with the DCA model are also shown in the table. The predicted terminal velocity using a mesh with two levels of successive refinement is 0.14 m/s. The prediction is within the experimental uncertainty. For the present simulations, the contact angle corrections due to the mesh dependent contact angle model are small, and the model did not produce better results than the DCA model. A similar conclusion was drawn by Saha and Mitra [37] who observed that the mesh-dependent contact angle model improved the results only marginally in simulations of microfluidic capillary flows.

4.2.4. Rolling vs. Sliding

The velocity vectors at various x-y cross-sections are now presented. The results presented are from the simulations using the coarse grid. Velocity vectors as the droplet moves at its terminal velocity are shown for a 7.5 μl water droplet on a 60° incline in Figure 13. Velocity vectors on x-y planes are shown in Figure 13 (a)-(c) at z = 0.0, 0.5 and 1.25 mm. A single circulating flow pattern is seen inside the droplet. The droplet is seen to roll on the surface. The center of the vortex is stationary at (x,y) = (0.58, 0.66) mm as the droplet is traversed along its z-axis (from z = 0.0 to z = 0.5 mm). The center moves to (0.65, 0.75) mm as the droplet surface is approached (Fig 15c). The center of mass of the droplet ($\bar{x}_m, \bar{y}_m, \bar{z}_m$) given by

$$(\bar{x}_m, \bar{y}_m, \bar{z}_m) = \left(\frac{\iiint_V x.\phi.dm}{\iiint_V \phi.dm}, \frac{\iiint_V y.\phi.dm}{\iiint_V \phi.dm}, \frac{\iiint_V z.\phi.dm}{\iiint_V \phi.dm} \right) \tag{9}$$

is (0.6, 0.67, 0.0) mm. This compares well with the vortex center location. This implies that the droplet center is stationary along the z-axis and changes only in a small region close to the air-water interface. A similar rolling flow pattern was observed experimentally using PIV by Sakai *et al.* [12].

The flow field in (white region) and around (gray region) the droplet is visualized using particle pathlines (Figure 14). The pathlines inside the droplet do not leave the droplet domain, as expected, and show a single, stable vortex inside the droplet. The flow of air far from the droplet surface is similar to flow over a sphere. The equivalent Reynolds number ($\rho_{air} V_T D/\mu_{air}$) based on the terminal velocity of the droplet is 30, which is in the laminar flow regime. In the reference frame of the droplet, an "attached vortex" is observed on the downwind side, which is similar to the expected Karman vortex flow pattern for $Re = 30$ [38]. The shear force exerted by the droplet on the air is large, which results in recirculation zones in the air close to the air-water interface.

5. CONCLUSIONS

Droplet motion on hydrophobic surfaces was studied by means of experiments and simulations. The advancing and receding contact angles of water droplets sliding on PTFE surfaces are characterized as a function of capillary number. The Seebergh and Berg correlation [36] best predicts the experimental advancing contact angle data, while a curve fit to the experimental measurements based on the Jiang *et al.* [35] model was used to describe the receding contact angle data.

A VOF-CSF numerical methodology based on a moving reference frame was developed to model the droplet motion on inclined hydrophobic surfaces. The model reduces computational time by an order of magnitude when compared to standard VOF droplet simulations in a stationary reference frame. The model was found to accurately predict the experimentally determined terminal velocity and droplet shape of water droplets moving on a PTFE surface. It was observed that the use of a dynamic contact angle (DCA) model for the contact angle boundary condition gave better predictions than the static contact angle (SCA) model. The recently published mesh-dependent contact angle model (MDCA) of Afkhami *et al.* [30] did not improve the predictions significantly. The prediction of terminal velocity for droplets on hydrophobic surfaces was observed to be highly sensitive to the contact angle model. The flow in and around the droplet was characterized. The droplet is seen to roll (rather than slide) based on the computed fluid motion inside the droplet.

6. ACKNOWLEDGEMENTS

The authors acknowledge financial support for this work from the Cooling Technologies Research Center, an NSF Industry/University Cooperative Research Center at Purdue University.

REFERENCES

[1] B. Bhushan, K. Koch, Y. C. Jung, Nanostructures for superhydrophobicity and low adhesion, Soft Matter, 4 (2008) 1799-1804.

[2] A.R. Wheeler, W.R. Throndset, R.J. Whelan, A.M. Leach, R.N. Zare, Y.H. Liao, K. Farrell, I.D. Manger, A. Daridon, Microfluidic device for single-cell analysis, Analytical Chemistry 75 (2003) 3581–3586.

[3] D. Erickson, D. Li, Integrated microfluidic devices, Analytica Chimica Acta, 507 (2004) 11-26.

[4] V. Dolnik, S. Liu, S. Jovanovich, Capillary electrophoresis on microchip, Electrophoresis, 21 (2000) 41–54.

[5] G.J.M. Bruin, Recent developments in electrokinetically driven analysis on microfabricated devices, Electrophoresis, 21 (2000) 3931–3951.

[6] G.H.W. Sanders, A. Manz, Chip-based microsystems for genomic and proteomic analysis, Trends in Analytical Chemistry 19 (2000) 364-378.

[7] M. Miwa, A. Nakajima, A. Fujishima, K. Hashimoto, T. Watanabe, Effects of the surface roughness on sliding angles of water droplets on superhydrophobic surfaces, Langmuir, 16 (2000) 5754–5760.

[8] G.D. Yarnold, The motion of a mercury index in a capillary tube, Proceedings of the Physical Society, 50 (1938) 540-552.

[9] R.F. Alle, P. R. Benson, Rolling drops on an inclined plane, Journal of Colloid Interface Science, 50 (1975) 250-253.

[10] M. Sakai, J. Song, N. Yoshida, S. Suzuki, Y. Kameshima, A. Nakajima, Direct observation of internal fluidity in a water droplet during sliding on hydrophobic surfaces, Langmuir, 22 (2006) 4906–4909.

[11] F. Song, PhD Thesis, Univ. of Akron, 2008.

[12] M. Sakai, A. Hashimoto, N. Yoshida, S. Suzuki, Y. Kameshima, A. Nakajima, Image analysis system for evaluating sliding behavior of a liquid droplet on a hydrophobic surface, Review of Scientific Instruments 78 (2007) 045103.

[13] S. Suzuki, A. Nakajima, M. Sakai, J. Song, N. Yoshida, Y. Kameshima, K. Okada, Slipping and Rolling Ratio of Sliding Acceleration for a Water Droplet Sliding on Fluoroalkylsilane Coatings of Different Roughness, Chemistry Letters, 37(2008) 58-59.

[14] M. Sakai, J. Song, N. Yoshida, S. Suzuki, Y. Kameshima, A. Nakajima, Relationship between sliding acceleration of water droplets and dynamic contact angles on hydrophobic surfaces, Surface Science, 600 (2006) L204-L208.

[15] P.R. Gunjal, V.V. Ranade, R.V. Chaudhari, Dynamics of drop impact on solid surface: Experiments and VOF simulations, AIChE Journal, 51 (2005) 59-78.

[16] J. Donea, A. Huerta, Finite Element Methods for Flow Problems. Wiley: Chichester, 2003.

[17] A. Brebbia, J.C.F. Telles, L.C. Wrobel, Boundary Element Techniques (Springer-Verlag, Berlin/Heidelberg), 1984.

[18] D.E. Finlow, P.R. Kota, A. Bose, Investigation of wetting hydrodynamics using numerical simulations, Physics of Fluids, 8 (1996) 302-309.

[19] P.D.M. Spelt, A level-set approach for simulations of flows with multiple moving contact lines with hysteresis, Journal of Computational Physics, 207 (2005) 389-404.

[20] C.W, Hirt, B.D.J. Nichols, Volume of fluid (VOF) method for the dynamics of free boundaries, Journal of Computational Physics, 39 (1981) 201-225.

[21] C. Gregor, P. Stojan, T. Lztok, Coupling of the interface tracking and the two-fluid models for the simulations of incompressible two phase-flow, Journal of Computational Physics, 171 (2001) 776–804.

[22] S. Afkhami, M. Bussmann, Height functions for applying contact angles to 3D VOF simulations, International Journal of Numerical Methods in Fluids 61 (2009) 827-847.

[23] S. Afkhami, Ph.D. Thesis, University of Toronto, 2008.

[24] S.R. Annapragada, J.Y. Murthy, S.V. Garimella, Droplet retention on an incline , International Journal of Heat and Mass Transfer (2010), in review.

[25] MATLAB: The language of technical computing, 2002, The MathWorks, Inc. Natick, MA.

[26] Fluent 6.3 Users Guide, Ansys Inc. Lebanon, NH, 1996.

[27] S. Hardt, F. Wondra, Evaporation model for interfacial flows based on a continuum-field representation of the source terms, Journal of Computational Physics, 227 (2008) 5871-5895.

[28] B. Lafaurie, C. Nardone, R. Scardovelli, S. Zaleski, Modelling merging and fragmentation in multiphase flows with SURFER, Journal of Computational Physics, 113 (1994) 134-147.

[29] E. Rio, A. Daerr, B. Andreotti, L. Limat, Boundary conditions in the vicinity of a dynamic contact line: experimental investigation of viscous drops sliding down an inclined plane, Physical Review Letters, 94 (2005) 02450.

[30] S. Afkhami, M. Bussmann, S. Zaleski, A mesh-dependent model for applying dynamic contact angles to VOF simulations Journal of Computational Physics, 228 (2009) 5370-5389.

[31] R.G. Cox, The dynamics of the spreading of liquids on a solid surface. Part 1. Viscous flow, Journal of Fluid Mechanics, 168 (1986) 169-194.

[32] O.V. Voinov, Hydrodynamics of wetting, Fluid Dynamics, 11 (1976) 714-721.

[33] P. Sheng, M. Zhou, Immiscible-fluid displacement: Contact-line dynamics and the velocity-dependent capillary pressure, Physical Review A, 45 (1992) 5694-5708.

[34] M. Bracke, F. De Voeght P. Joos, The kinetics of wetting: the dynamic contact angle, Progressions in Colloid Polymer Science 79 (1989) 142-149.

[35] T. Jiang, S. Oh, J.C. Slattery, Correlation for dynamic contact angle, Journal of Colloid and Interface Science, 69 (1979) 74-77.

[36] J. E.Seebergh, J. C. Berg, Dynamic wetting in the low capillary number regime, Chemical Engineering Science, 47 (1992) 4455-4464.

[37] A. A. Saha, S. K. Mitra, Effect of dynamic contact angle in a volume of fluid (VOF) model for a microfluidic capillary flow, Journal of colloid and interface science, 339 (2009) 461-480.

[38] H. Niazmand, M. Renksizbulut, Flow past a spinning sphere with surface blowing and heat transfer, Journal of Fluids Engineering, 127 (2005) 163-171.

FIGURE CAPTIONS

Figure 1. Experimental setup for droplet-sliding experiments.

Figure 2. Time step loop for the numerical calculations.

Figure 3. Initial shape of the droplet (identified with the $\alpha = 0.5$ line) and the mesh surrounding the droplet shown at the symmetry plane.

Figure 4. The three contact angle boundary conditions implemented in this work plotted as a function of the local capillary number.

Figure 5. Water droplet images at inclinations (β) of 30°, 45° and 60° for droplet sizes of 5, 7.5 and 10 μl.

Figure 6. Measured contact angles as a function of capillary number.

Figure 7. Comparison of various dca models with experimental measurements of θ_{adv}.

Figure 8. 2d mesh for droplet reference frame simulation used for the validation exercise. The initialized droplet shape is shown in red.

Figure 9. Location of droplet advancing edge, receding edge and reference frame velocity as a function of time.

Figure 10. Comparison of velocity profiles inside the droplet at x = 0.9 mm from the receding edge; this x-location is marked in the inset showing velocity vectors in the droplet.

Figure 11. Comparison of computed and experimentally measured droplet shapes. $V_{drop} = 10$ µl and β = 45°. Numerical simulation at $\alpha = 0.5$ (red outline), experimental measurement (grayscale image).

Figure 12. Droplet contact line from numerical predictions. The contact line is colored with the contact angles (degrees) along the contact line.

Figure 13. Velocity vectors for fully developed flow in a 7.5 μl water droplet moving down a 60° incline at terminal velocity along (a)-(c) *xy* planes (z = 0 mm, *z* = 0.5 mm and *z* = 1.25 mm).

Figure 14. Pathlines for fully developed flow in and around a 7.5 µl droplet on a 60 degree incline at z = 0 mm (white – water, gray – air).

Table 1. Empirical DCA models available in the literature.

Model	*Correlation*
Bracke *et al.* [34]	$\frac{\cos\theta_0 - \cos\theta(t)}{2(1+\cos\theta_0)} = Ca^{1/2}$
Jiang *et al.* [35]	$\frac{\cos\theta_0 - \cos\theta(t)}{\cos\theta_0 + 1} = \tanh\left(4.96Ca^{0.702}\right)$
Seebergh and Berg [36]	$\frac{\cos\theta_0 - \cos\theta(t)}{\cos\theta_0 + 1} = 2.24Ca^{0.54}$

Table 2. Comparison of simulation results in the stationary reference and droplet reference frames.

Parameter	*Stationary reference*	*Droplet reference*
Terminal velocity (m/s)	0.27	0.27
Number of computational cells required	20,000	2,800
Simulation time (minutes)	350	50

Table 3. Comparison of predicted terminal velocities with experimental results.

Parameter	*Experiment*	*Predicted*	*Deviation*
Volume = 5.0µl, $\beta = 60°$	0.04±0.01 m/s	0.06±0.02 m/s	50%
Volume = 7.5µl, $\beta = 60°$	0.12±0.01 m/s	0.14±0.02 m/s	17%
Volume = 10.0µl, $\beta = 60°$	0.23±0.01 m/s	0.22±0.02 m/s	4%

Table 4. Comparison of predicted and experimentally measured droplet length, height and velocity.

Parameter	*Numerical*	*Experimental*
Droplet length (mm)	2.54±0.088	2.54±0.005
Droplet height (mm)	1.79±0.088	1.80±0.005
Droplet velocity (m/s)	0.14±0.088	0.12±0.005

Table 5. Comparison of predicted droplet length, droplet height and terminal velocities for volume = 7.5μl, β = 60° using various contact angle models.

Parameter	*Droplet length*	*Droplet height*	*Terminal Velocity*	
			Coarse Mesh	*Fine Mesh*
SCA model	2.53 mm	1.80 mm	0.04±0.02 m/s	-
DCA model	2.54 mm	1.79 mm	0.14±0.02 m/s	0.14±0.02 m/s
MDCA model	2.54 mm	1.79 mm	0.14±0.02 m/s	0.14±0.02 m/s

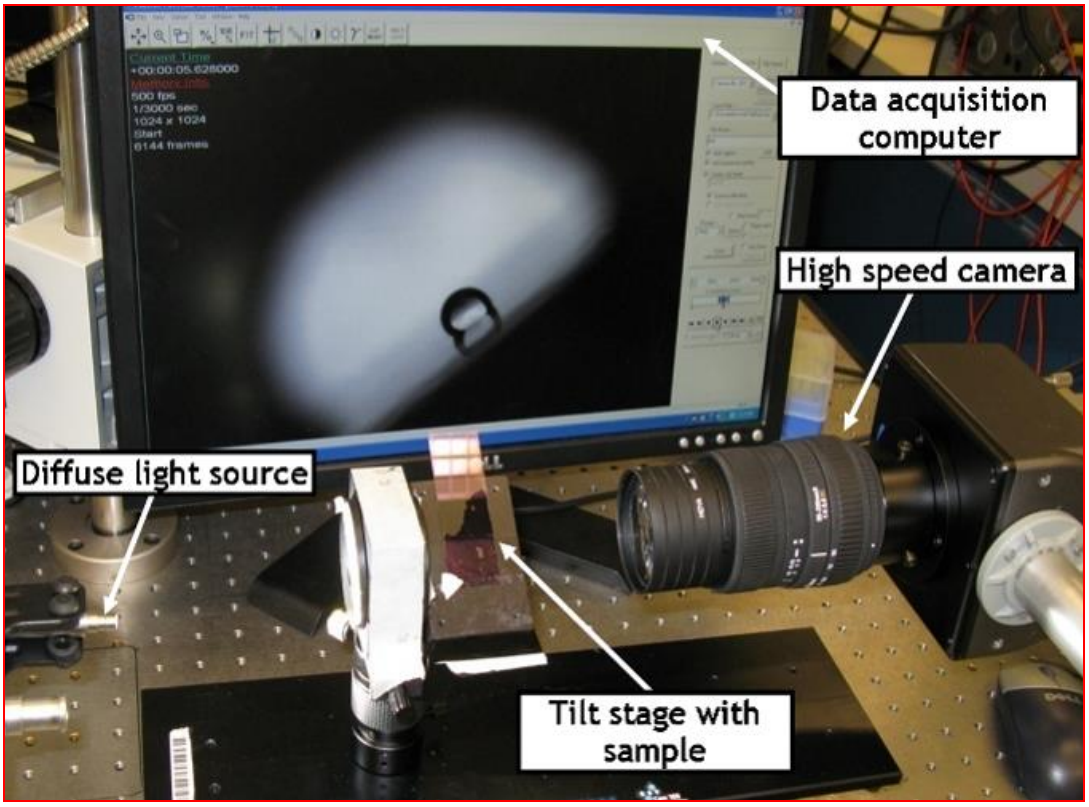

Figure 1. Experimental setup for droplet-sliding experiments.

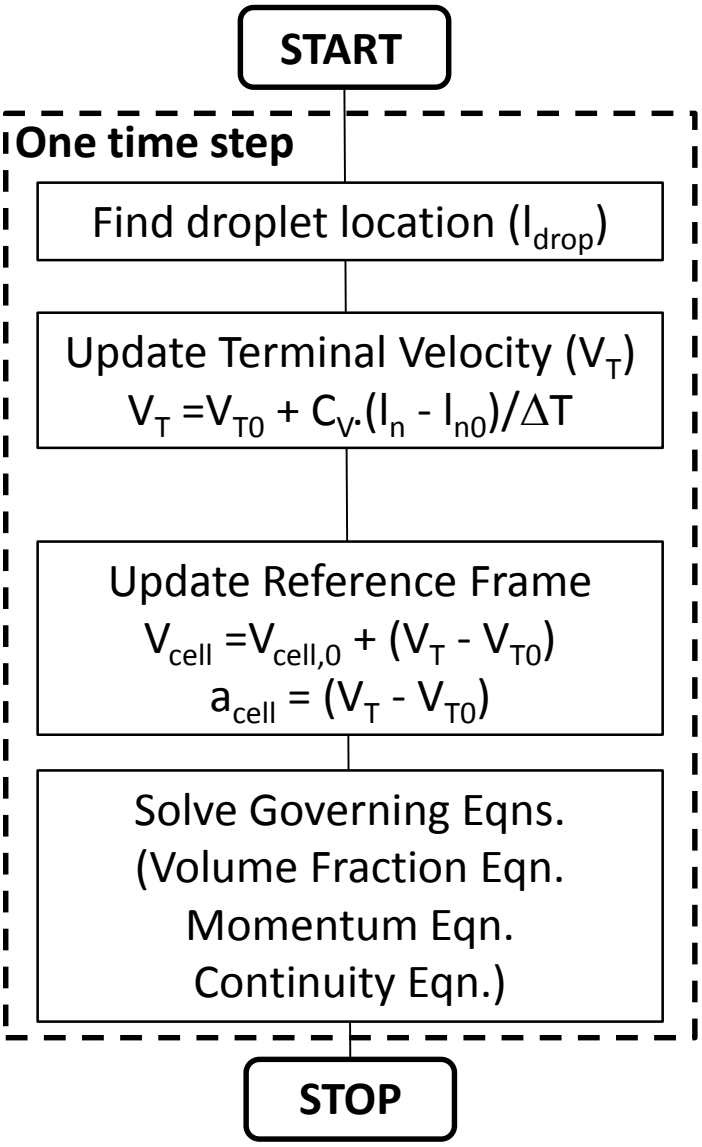

Figure 2. Time step loop for the numerical calculations.

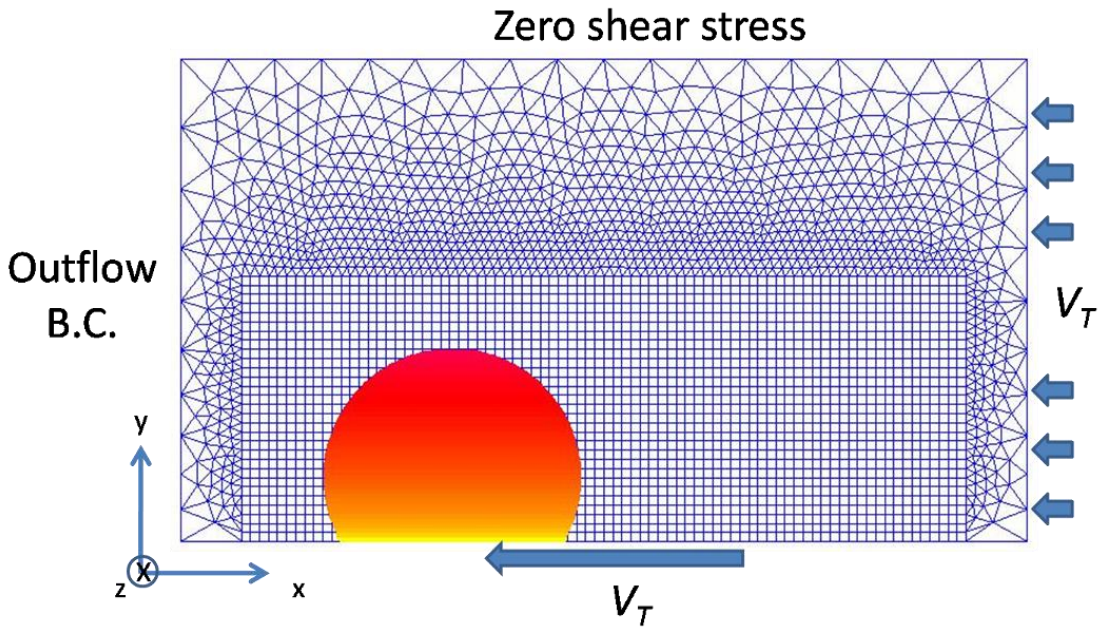

Figure 3. Initial shape of the droplet (identified with the $\alpha = 0.5$ line) and the mesh surrounding the droplet shown at the symmetry plane.

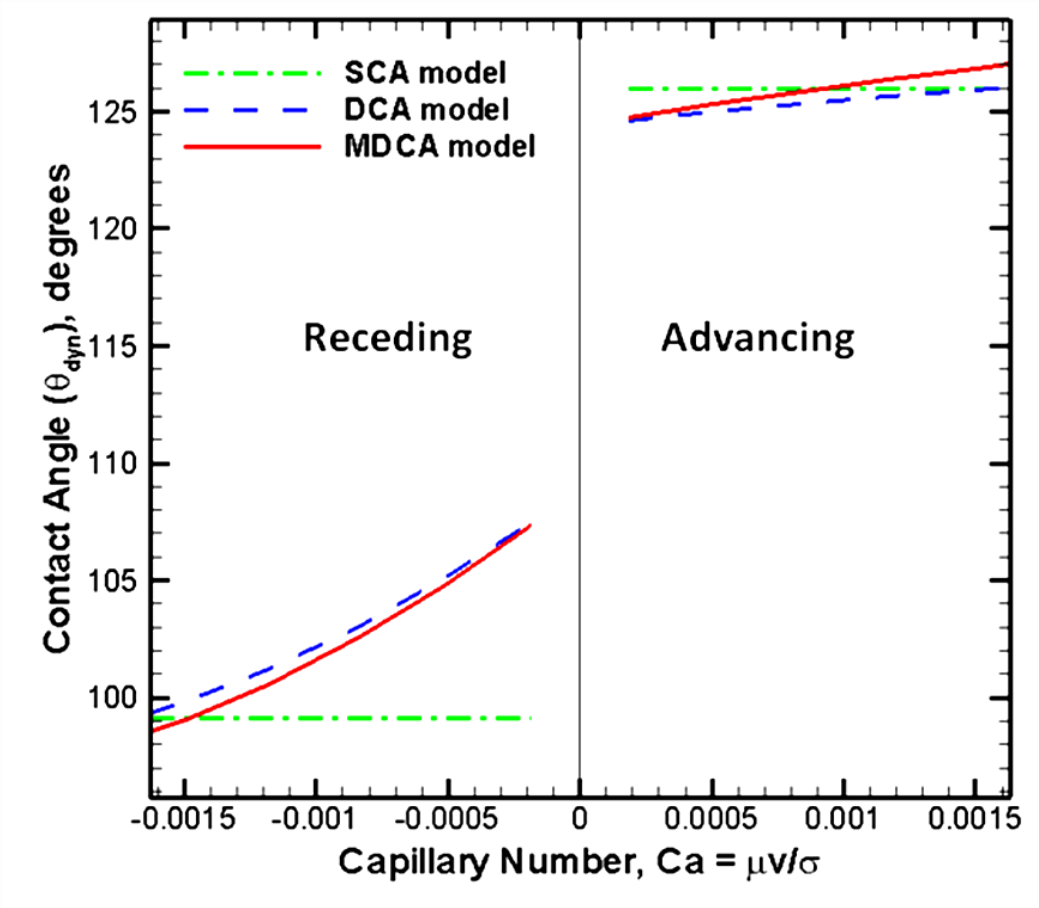

Figure 4. The three contact angle boundary conditions implemented in this work plotted as a function of the local capillary number.

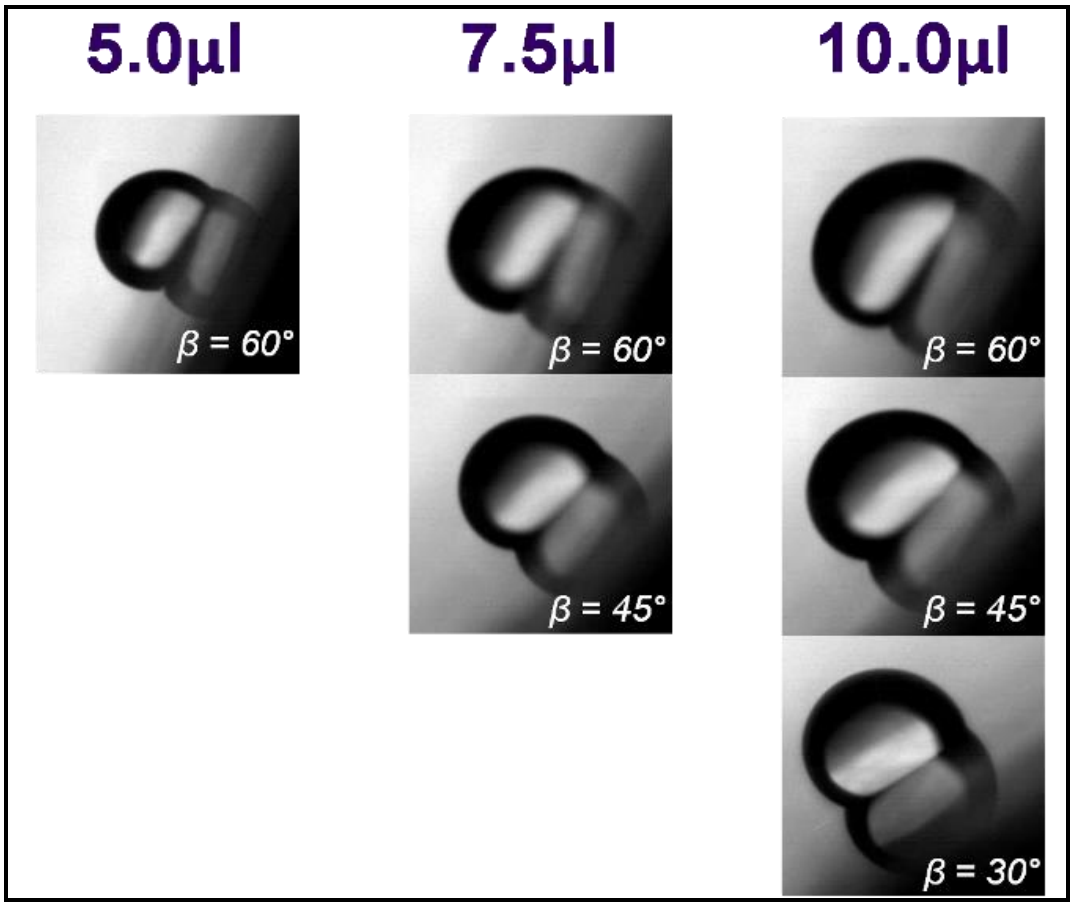

Figure 5. Water droplet images at inclinations (β) of 30°, 45° and 60° for droplet sizes of 5, 7.5 and 10 μl.

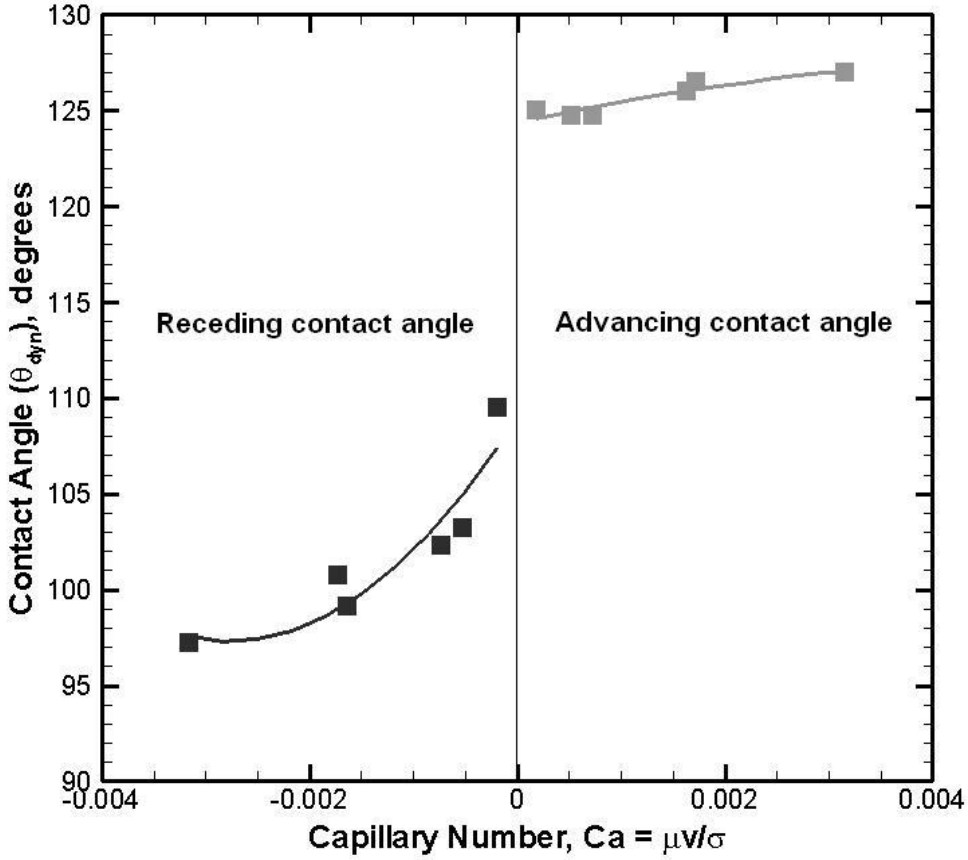

Figure 6. Measured contact angles as a function of capillary number.

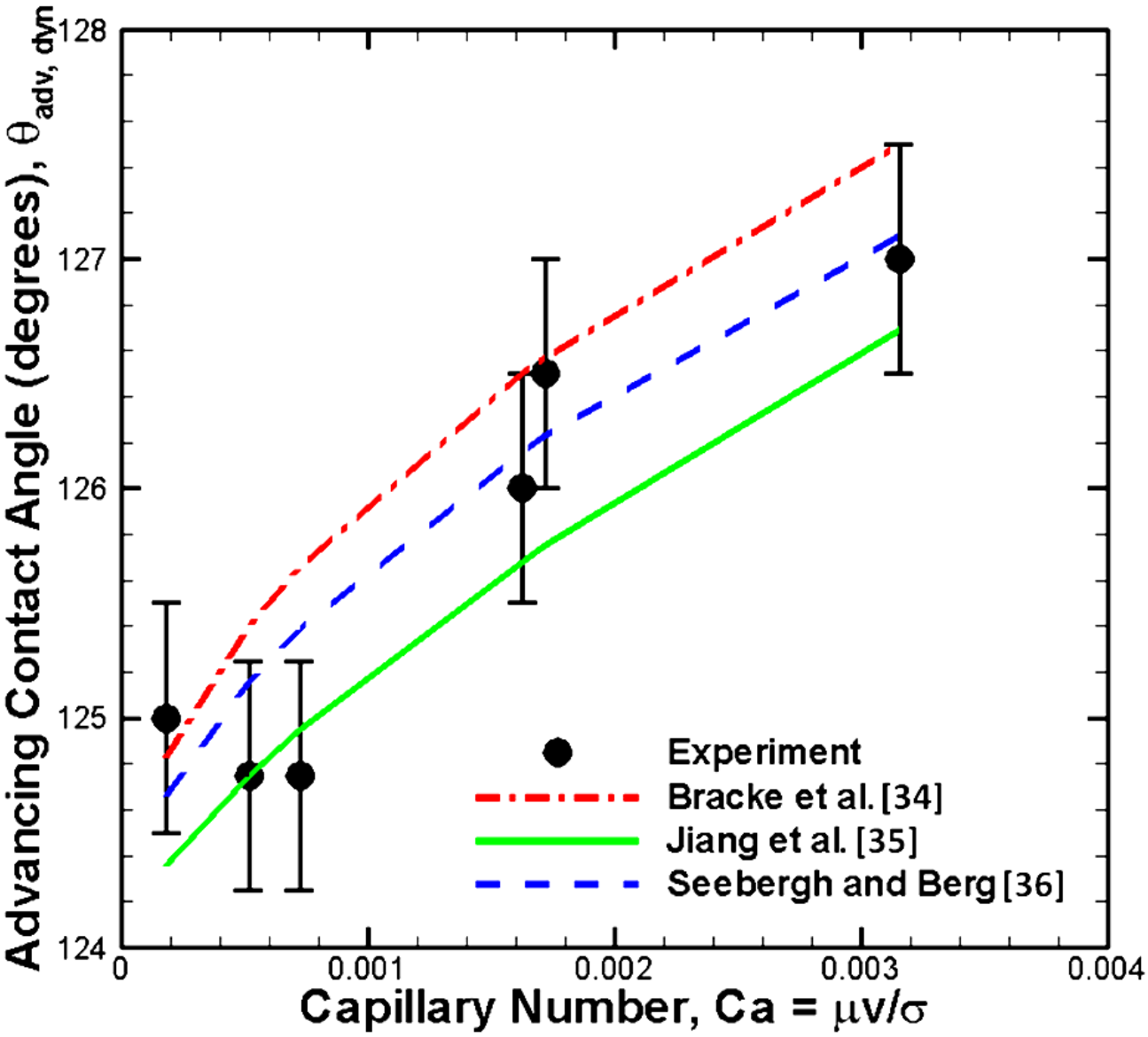

Figure 7. Comparison of various DCA models with experimental measurements of θ_{adv}.

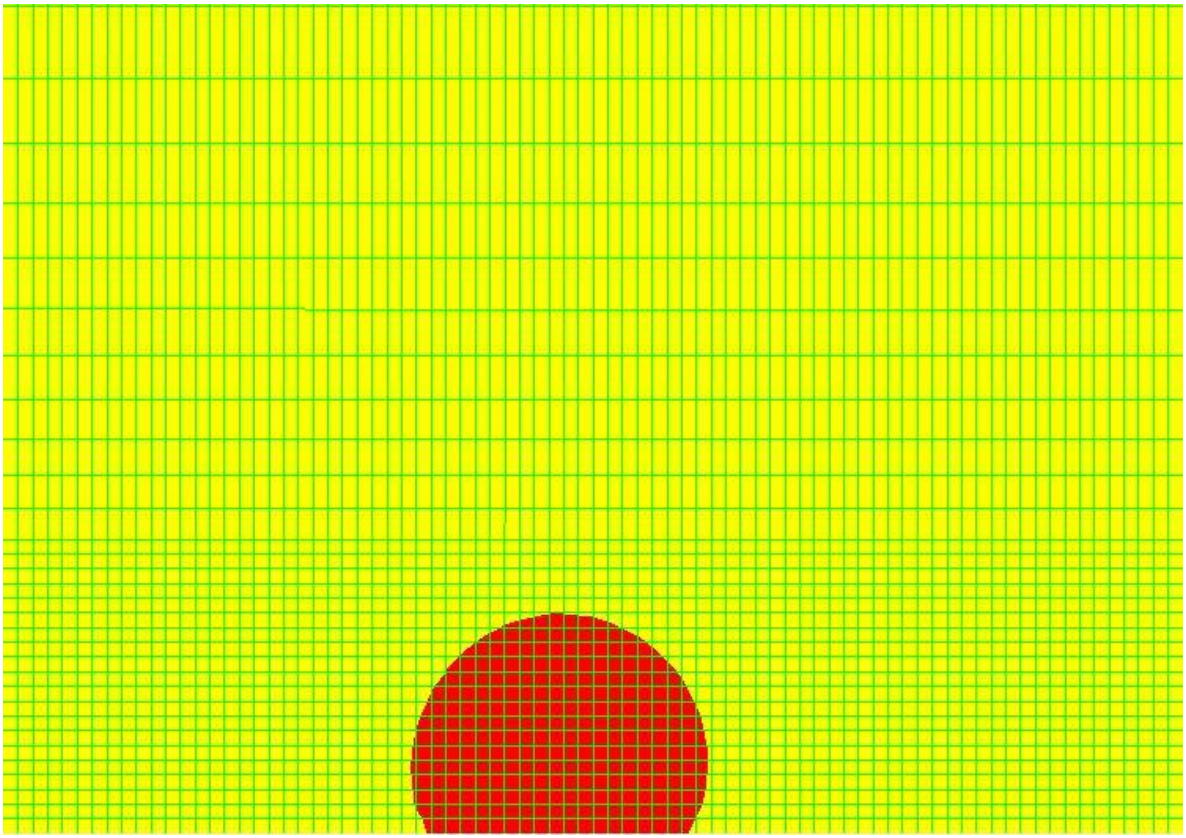

Figure 8. 2D mesh for droplet reference frame simulation used for the validation exercise. The initialized droplet shape is shown in red.

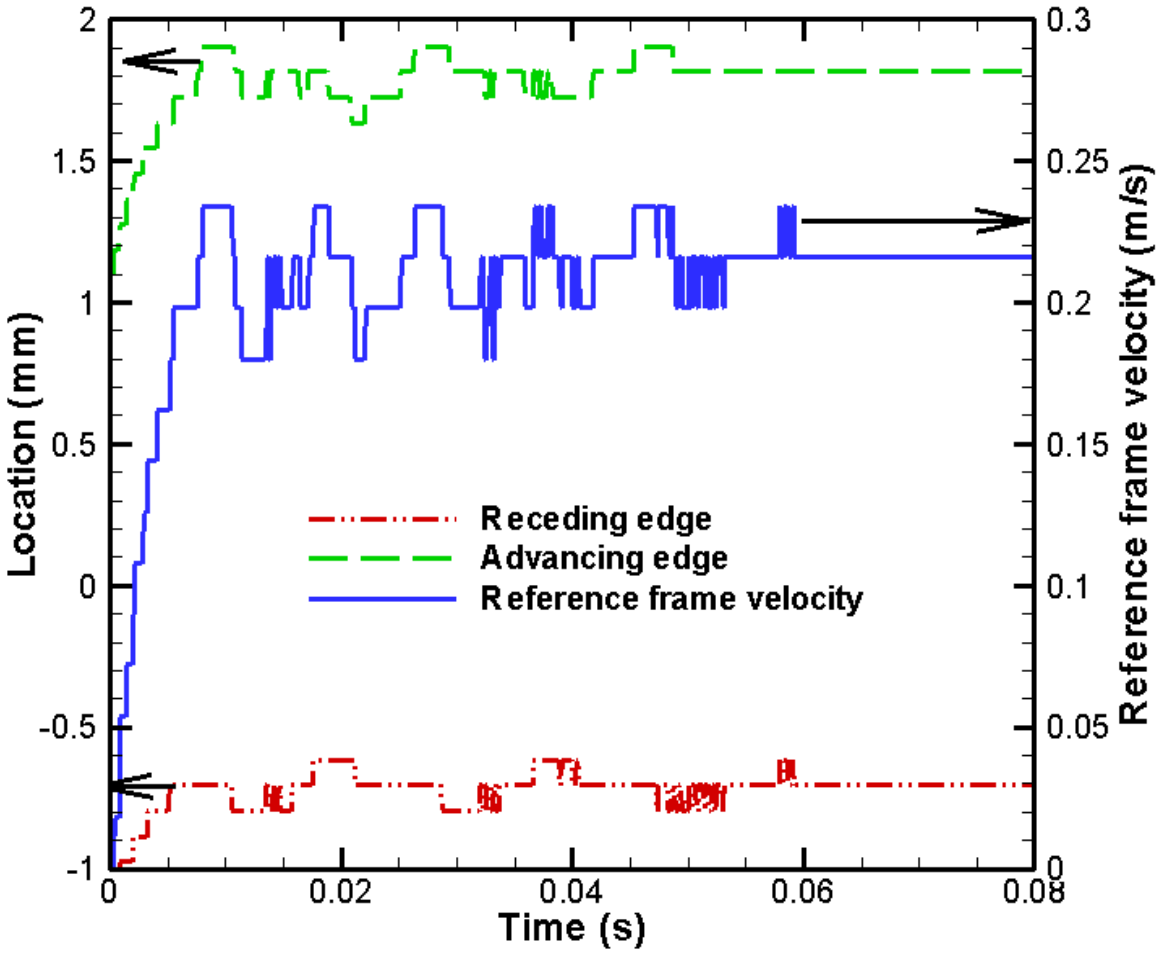

Figure 9. Location of droplet advancing edge, receding edge and reference frame velocity as a function of time.

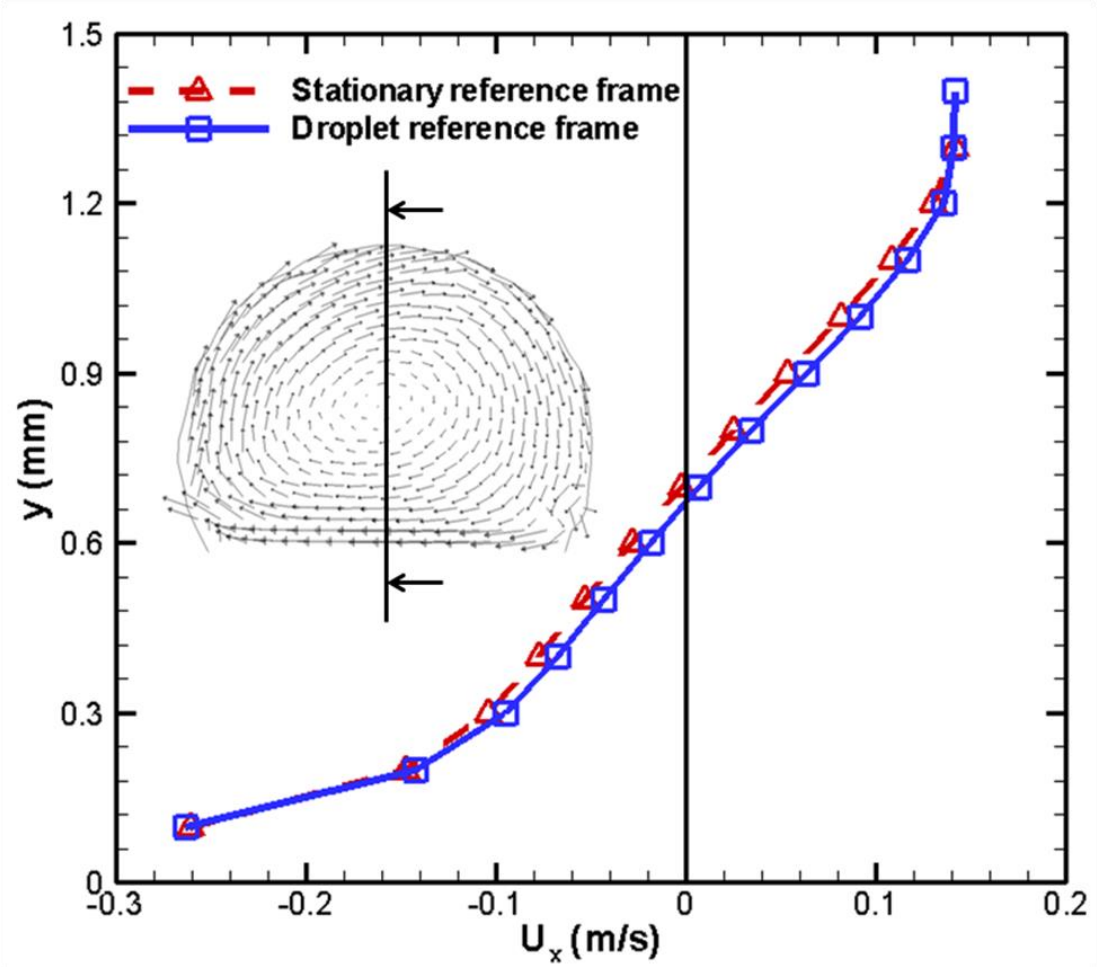

Figure 10. Comparison of velocity profiles inside the droplet at x = 0.9 mm from the receding edge; this x-location is marked in the inset showing velocity vectors in the droplet.

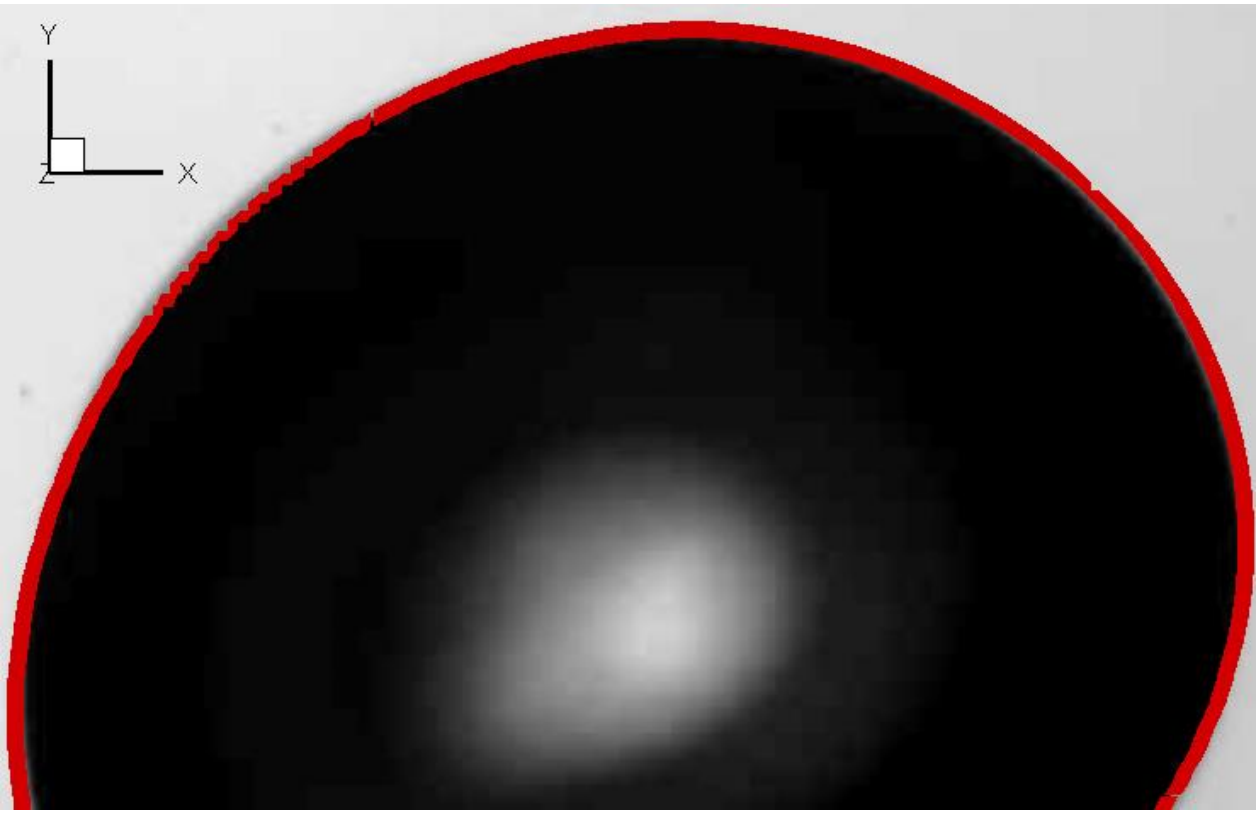

Figure 11. Comparison of computed and experimentally measured droplet shapes. V_{drop} = 10 μl and β = 45°. Numerical simulation at α = 0.5 (red outline), experimental measurement (grayscale image).

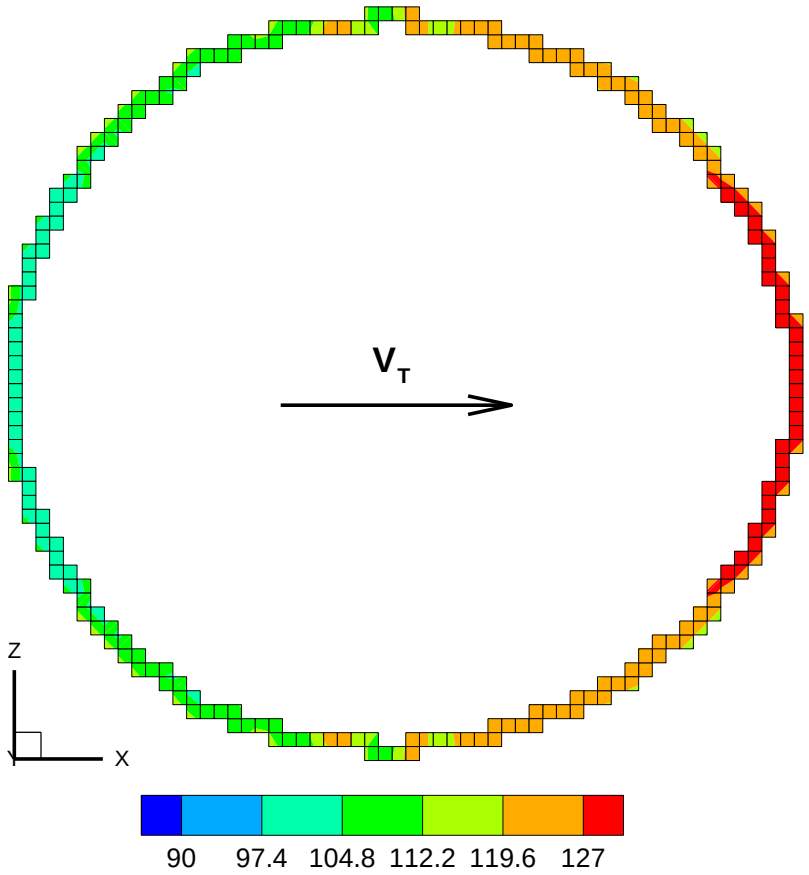

Figure 12. Droplet contact line from numerical predictions of 10 µl droplet moving down a $\beta = 45°$ incline. The contact line is colored with the contact angles (degrees) along the contact line.

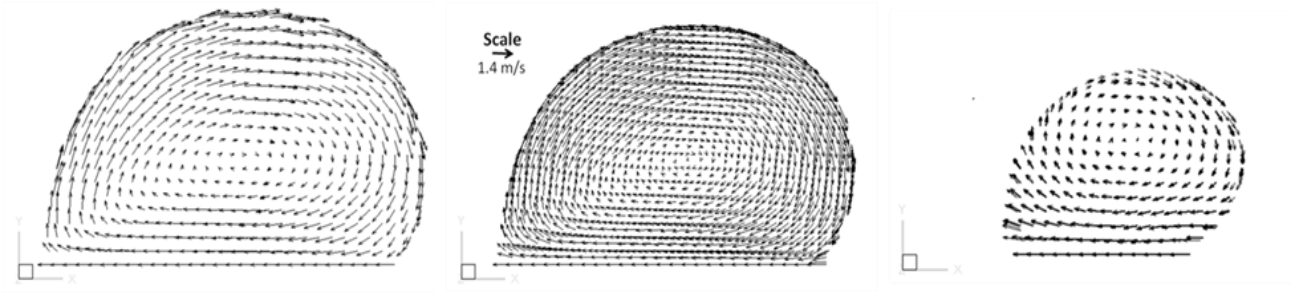

(a) (b) (c)

Figure 13. Velocity vectors for fully developed flow in a 7.5 μL water droplet moving down a 60° incline at terminal velocity along (a)-(c) *xy* planes (z = 0 mm, z = 0.5 mm and z = 1.25 mm).

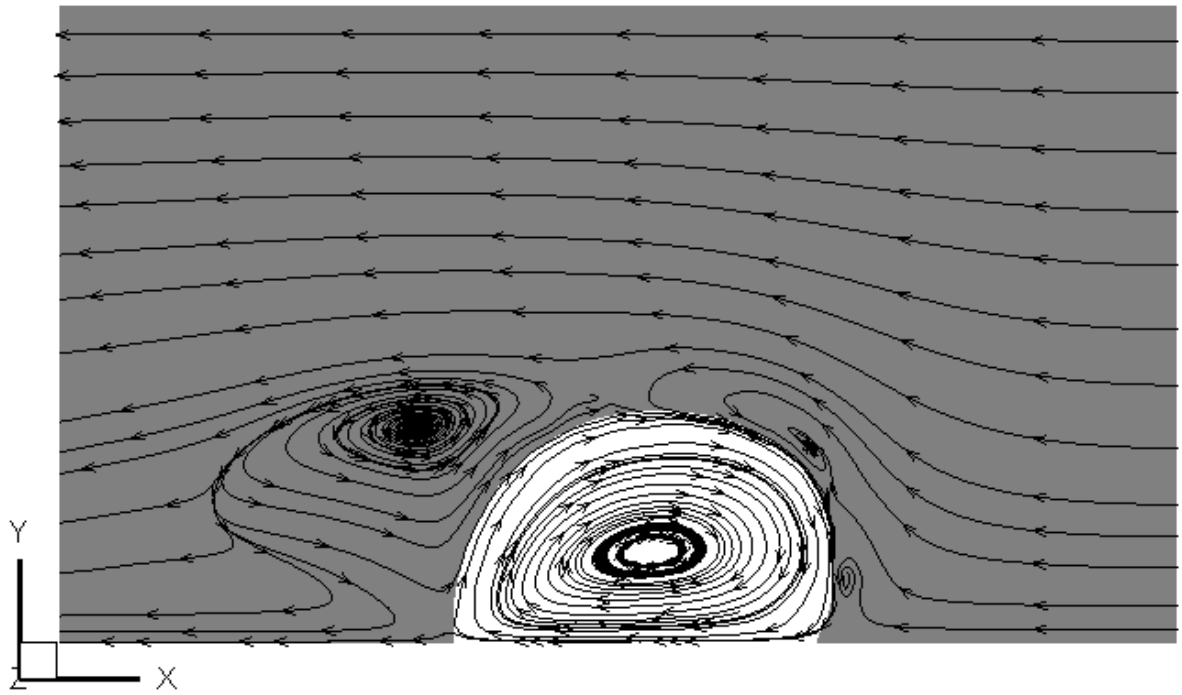

Figure 14. Pathlines for fully developed flow in and around a 7.5 µl droplet on a 60° incline at z = 0 mm (white – water, gray – air).